

1 Rhomboid beach pattern: a laboratory investigation

O. Devauchelle,¹ L. Malverti,¹ É. Lajeunesse,¹ C. Josserand,² P.-Y. Lagrée,²

F. Métivier¹

¹Laboratoire de Dynamique des Fluides
Géologiques, Institut de Physique du Globe
de Paris, France.

²Institut Jean Le Rond d'Alembert –
CNRS, Université Pierre et Marie Curie,
France.

2 **Abstract.** The formation of beach rhomboid pattern by swash is inves-
3 tigated experimentally. This centimeter-scale structure is classically inter-
4 preted as the mark of stationary gravity waves generated by obstacles in su-
5 percritical flows. However, thanks to the use of water-based fluids of vari-
6 ous viscosity, our experiments show that a rhomboid pattern can develop in
7 subcritical flows. Its angle is primarily a function of the Froude number, as
8 suggested by Woodford, but our data do not support his classical model, nor
9 do they support any of the existing theories. The slowness of the rhombus
10 motion indicates that it is not simply the mark of a hydraulic phenomenon,
11 but rather results from the coupling between the water flow and sediment
12 transport.

1. Introduction

13 When observing the surface of a beach, one can very often notice a regular crossed
14 pattern composed of a network of diamond-shaped sand structures (see figure 1). Their
15 typical size lies from a few centimeters to a few tens of centimeters, while their height
16 rarely exceeds a few millimeters [Stauffer *et al.*, 1976]. They usually appear after the
17 swash, when water returns to sea, hence the name “*backwash mark*” given by Johnson
18 [1919]. Almost every author refers to this ubiquitous pattern in their own way [Allen,
19 1982]. In the following, we will use the name *rhomboid pattern*.

20 To our knowledge, the first contribution on the subject may be credited to Williamson
21 [1887], whose primary interest was sedimentary records of rhomboid patterns. Indeed,
22 Thompson [1949], Singh [1969] and Collinson and Thompson [1982] reported similar
23 structures in ancient rocks. We are not aware of any other description. Despite this
24 rarity, most studies of present beach rhomboid pattern were motivated by its potential
25 utility as an environmental indicator for ancient shorelines [Hoyt and Henry, 1963].

26 The majority of publications on the subject refer to small-scale structures (see Otvos
27 [1965] and Stauffer *et al.* [1976] among others, or Allen [1982] for a complete review). How-
28 ever, McMullen and Swift [1967] and Morton [1978] show impressive aerial photographs
29 of at least 10 m-large rhomboid structures, first reported by Straaten [1953]. This sug-
30 gests that understanding the formation of beach rhomboid pattern could shed light on a
31 more general problem in geomorphology, namely the growth and migration of bedforms,
32 such as ripples, dunes, banks or alternate bars. Rhomboidal structures resembling the
33 pattern we describe have also been observed in deep (as compared to the bedform size)

and turbulent flows [*Gyr and Schmid*, 1989; *Best*, 1992; *Venditti et al.*, 2005]. In each of these experiments, the rhomboid shapes appeared on the bed without any other preexisting perturbation and were regular features. The rhombi observed by these authors then transformed into transverse sandwaves. We do not know if these structures result from the same mechanism as the experimental pattern described in the present paper.

A number of theories have been proposed to explain the formation of the beach rhomboid pattern (see 1). The first quantitative theory is due to *Woodford* [1935], who noted the likeness between the rhomboid pattern and stationary waves in supercritical open-channel flows. As explained in the caption of figure 2, the inclination α of the waves with respect to the mean flow direction is easily determined:

$$\alpha = \arcsin \frac{1}{F}, \quad (1)$$

where F is the Froude number (if U , D and g are the mean velocity of the flow, its mean depth and the acceleration of gravity respectively, then $F = U/\sqrt{gD}$). *Woodford* assumes that the rhomboidal structures the swash carves into the sand are passive marks of these waves, and thus should present the same angle.

Chang and Simons [1970] were the first to write a full system of equations which includes both the water flow and the sediment transport. By doing so, they introduced the idea that rhomboid patterns could result from the coupled interaction between water flow and sediment transport. However, even though *Chang and Simons* [1970] have written a fully coupled system of equations, they later neglect sediment transport, thus returning to *Woodford's* model. They would have ended up with *Woodford's* formula but for a mistake in their analysis (see Appendix).

56 The question of the perturbation from which a rhomboid pattern originates was raised
57 early in the history of analysis of the pattern. Otvos suggested that the elements in
58 rhomboids were associated with triggering obstacles on the bed (“*shell fragments, pebbles,*
59 *plant-clumps, et caetera*” [Otvos, 1965, 271]). However, on natural surfaces these obstacles
60 will be arranged at random, in contradiction with a striking feature of rhomboid pattern,
61 namely its regular wavelength (see figure 1). This was already pointed out by Woodford,
62 who warned the reader about the “*V-shaped grooves which spread from the snouts of*
63 *partly buried sand crabs*” [Woodford, 1935, 518]. Karcz and Kersey [1980] performed
64 experiments on well-sorted sand, and were able to generate regular rhomboid pattern,
65 thus showing that this pattern can appear spontaneously without any obstacle. Later,
66 Daerr *et al.* [2003] reported the same pattern on a plate covered with a uniform sediment,
67 when it is withdrawn at constant angle and velocity from a bath of still water, again
68 without any obstacle.

69 In Woodford’s theory, the rhomboid pattern has to be generated by some obstacle.
70 Allen’s remark “*It appears that symmetrically interfering oblique hydraulic jumps can*
71 *also be produced in channelized flows of sufficient breadth without deflecting obstacle*”
72 [Allen, 1982, 399] is probably based on the experiments described by Chang and Simons
73 [1970], during which regularly-spaced fronts were formed. However, we believe this remark
74 is somewhat misleading, since the “*hydraulic jumps*” of the experiment were formed in
75 interaction with the granular bed. Stationary hydraulic jumps, without this interaction,
76 do not present any characteristic wavelength and must be triggered by obstacles. To
77 our knowledge, regular rhombi such as the ones of Chang and Simons [1970] have been

78 observed only in situations where the flow interacts with its granular substrate, as in the
79 experiments presented here.

80 More recently, *Stauffer et al.* [1976] proposed a radically different theory based on the
81 underground flow induced by the beach drainage. It has not lead to quantitative pre-
82 dictions of the rhomboids characteristics, and thus cannot be tested against experiments
83 or field measurements. Later, *Devauchelle et al.* [2007] showed that the moving contact
84 line (the intersection of the water surface with the sediment) is not responsible for the
85 rhomboid pattern, at least in the experiments of *Daerr et al.* [2003].

86 In order to test the above theories, we have performed a series of laboratory experiments
87 in a laminar channel. The measurements focus on the geometrical properties of the
88 pattern, namely its angle α and its wavelength λ , which are critical for quantitative
89 comparison against theory. The velocity of the experimental bedforms then provides
90 some insight about the pattern dynamics. Preliminary experiments in a smaller channel
91 were described in *Devauchelle et al.* [2008].

2. Description of the experiment

2.1. Experimental arrangements and procedure

92 We performed this set of experiments in a flume of width $W = 9.6$ cm and length
93 $L = 240$ cm (figure 3). The flume reposed on a tilted plane which allowed us to vary
94 the mean bed slope S , measured with a digital inclinometer of accuracy 0.1° . The flume
95 was filled with a 5.5 cm-thick bed of glass beads of density $\rho_s = 2500$ kg.m⁻³. The
96 sediment grain diameter distribution (figure 4) had a geometric standard deviation of
97 $\sigma_g = \sqrt{d_{84}/d_{16}} = 1.2$, where 84% (respectively 16%) of the grains have a diameter below

98 d_{84} (respectively d_{16}) [Vanoni, 2006]. In the following, we will consider this well-sorted
 99 sediment as monodisperse, with a median grain diameter $d_s \approx 75 \mu\text{m}$.

100 A pump injected the fluid at the flume inlet. The flow discharge Q_w remained constant
 101 during each experimental run, and was measured with a flowmeter of accuracy 0.01ℓ
 102 min^{-1} . The fluid was either pure water or a mixture of water and glucose, which mass
 103 proportion varied from 0% to 50%. The slope ranged from 0.008 to 0.052 (that is from
 104 0.46° to 3°), the water discharge from $0.24 \ell \text{ min}^{-1}$ to $4.42 \ell \text{ min}^{-1}$ and the fluid viscosity
 105 from 10^{-6} to $5.6 \times 10^{-6} \text{ m}^2\text{s}^{-1}$.

106 We also measured the sediment discharge Q_s , by continuously weighing a tank fitted
 107 with an overflow, into which were collected both the sediment and the water leaving the
 108 channel. However, this measurement was only possible when the sediment discharge was
 109 large enough to be measured during the time of an experiment.

110 The influence of glucose on surface tension is fairly moderate. For instance, adding 17%
 111 of glucose to water produces a surface tension increase of less than 2%, while adding 55%
 112 of glucose creates an increase of about 5% [Docoslis et al., 2000]. We will thus approximate
 113 the surface tension of the mixture by the pure water value, $\sigma = 74 \times 10^{-3} \text{ Nm}^{-1}$. It was
 114 not measured during the experiments.

115 The Reynolds number is defined as

$$116 \quad \text{Re} = \frac{UD}{\nu} = \frac{Q_w}{W\nu}, \quad (2)$$

117 where D and U are the flow depth and the average water velocity respectively. The
 118 Reynolds number below which an open channel flow may be considered laminar is typically
 119 500 [Orszag and Kells, 1980]. Since it varied between 9.9 and 420 during our experiments,
 120 we will hereafter assume that the flow is laminar.

121 The flow depth was too small to be measured with sufficient precision. Instead, it can be
 122 approximated by the depth of a Nusselt film with a parabolic velocity profile, as confirmed
 123 by *Malverti et al.* [2008] with the same experimental set-up. The mass and momentum
 124 balance for a Nusselt film reads

$$125 \quad Q_w = WDU, \quad gS = \frac{3\nu U}{D^2}, \quad (3)$$

126 where g is the acceleration of gravity. Based on the above equations, the water depth
 127 ranged between 0.89 mm and 5.5 mm during our experiments, while the averaged velocity
 128 varied between 0.30 ms^{-1} and 0.037 ms^{-1} .

129 The experimental procedure was the following. An initially flat bed was prepared by
 130 sweeping a rake over the sediment surface, the tilt and height of the rake being constrained
 131 by two rails parallel to the channel. This flat bed is referred to as the *base state* in the
 132 following. Under certain conditions, a rhomboidal bedform appeared at the sediment
 133 surface a few seconds after the flow had started (see section 3.1). The rhomboid pattern
 134 was extremely flat (typically less than 1 mm), and usually disappeared (or at least became
 135 even fainter) when the water flow stopped. In order to make these faint bedforms visible,
 136 the bed was lit up with a light beam directed horizontally through one of the sides. We
 137 then recorded frames of these patterns at regular time intervals with a camera fixed above
 138 the flume (figure 3). We measured the opening angle α , the longitudinal and transverse
 139 wave length (λ_x and λ_y respectively) and the velocity of the bedforms. The angle α
 140 corresponds to the angle between the crest line of a bedform and the direction of the flow
 141 (see figure 3). The longitudinal wavelength λ_x was estimated by counting the number of
 142 structures along the flume bed in the field of view. The same method was used to estimate
 143 λ_y . The pattern wavelength λ , which represents the distance between two opposite sides

144 of a rhombus, is given by

$$145 \quad \lambda = \frac{1}{\sqrt{1/\lambda_x^2 + 1/\lambda_y^2}}. \quad (4)$$

2.2. Dimensional analysis

146 Ten experimental parameters are likely to influence the rhomboid pattern:

- 147 • the water discharge Q_w ;
- 148 • the slope S ;
- 149 • the fluid viscosity ν ;
- 150 • the acceleration of gravity g ;
- 151 • the fluid surface tension σ ;
- 152 • the density of water ρ_w , and that of the grains ρ_s ;
- 153 • the median grain size d_s ;
- 154 • the width and the length of the channel, respectively W and L .

155 The above list includes only the parameters on which we have a direct control. Of
 156 course, flow parameters such as the velocity U or the depth D are likely to influence
 157 the pattern shape. Nevertheless, they are selected by the arrangement itself once the
 158 operator sets the discharge, the slope and the viscosity. Consequently, in the dimensional
 159 analysis, they are experimental results to be considered in the same way as the bedforms
 160 characteristics. Below, the influence of the flow depth and velocity on the bed pattern
 161 is expressed through dimensionless numbers which can be evaluated from the primary
 162 quantities listed above.

163 According to the so-called Pi theorem [*Barenblatt*, 1996], and since there are three
 164 dimensions of interest (namely length, time and mass), the results are functions of any

165 set of seven independent non-dimensional numbers. Given that only three dimensional
 166 parameters varied during the experiment (Q_w , S and ν), it is natural to define a set of
 167 three varying non-dimensional numbers, and four non-dimensional constants. We first
 168 define the following constants (the symbol \equiv denotes a definition):

- 169 • the density ratio $R \equiv (\rho_s - \rho_w)/\rho_w \approx 1.50$;
- 170 • the channel aspect ratio $R_c \equiv W/L \approx 0.040$;
- 171 • the non-dimensional grain size $R_s \equiv d_s/W \approx 7.81 \times 10^{-4}$;
- 172 • the Bond number $Bo \equiv \rho g W^2/\sigma \approx 1240$.

173 The Bond number is the squared ratio of the channel width to the capillary length. The
 174 experimental results are likely to depend on the above constants, but our experiments can
 175 provide no information about their influence. Finally, we choose three varying independent
 176 numbers:

- 177 • the channel slope S ;
- 178 • the Froude number $F \equiv (SQ_w/(3W\nu))^{1/2} = U/\sqrt{gD}$;
- 179 • the Shields parameter $\theta \equiv (3\nu Q_w S^2/(gWR^3 d_s^3))^{1/3} = \tau/((\rho_s - \rho)gd_s)$, where τ is the
 180 shear stress exerted by the flow on the bed;

181 The above definitions involve only experimental parameters which we can measure di-
 182 rectly. Of course, they correspond to the classical definitions through equation (3). The
 183 Froude number F relates inertial forces to pressure, when the pressure field is hydrostatic.
 184 It is also the ratio of celerity of the surface gravity wave to flow velocity, to the extent
 185 that the shallow water approximation holds. The Shields parameter is the ratio of the
 186 viscous force exerted by the flow on a bed particle to its immersed weight. There exists a
 187 threshold value of the Shields number θ_c below which no sediment is transported. During

188 our experiments, the flow was slow enough and the particles large enough for the grains to
 189 remain near the bed during transport. As a consequence, the dominant transport mode
 190 is bedload [*Malverti et al.*, 2008], which is usually characterized by the Shields parameter
 191 [*Vanoni*, 2006].

192 The choice of the above parameters is arbitrary, any set of three independent and varying
 193 quantities would be sufficient to describe the results. However, we define three additional
 194 quantities for illustrative purpose. They can be derived from the initial set of parameters:

- 195 • the Reynolds number defined in section 2.1, which satisfies $Re = 3F^2/S$;
- 196 • the Weber number $We \equiv (\theta R R_s F)^2 Bo/S = \rho U^2 D/\sigma$;
- 197 • the cross-section aspect ratio of the flow $R_f \equiv \sqrt{We/Bo}/F = D/W$.

198 The Reynolds number compares viscous forces to inertia, while the Weber number
 199 compares the influence of capillary forces to fluid inertia.

3. Results

3.1. Description of the bedforms

200 When the water pump is turned on, the flow fills the channel, without inducing any
 201 visible deformation of the initial bed. For a very small discharge, no sediment grain moves.
 202 Above a certain discharge, a few grains move at the sediment surface, indicating that the
 203 Shields parameter is above the threshold. The system may then evolve in three different
 204 ways.

205 In some cases (typically for high slope S and high outflow Q_w), the bed remains flat
 206 and homogeneous, despite a visible sediment flux along the flow direction x . The system
 207 is then stable.

208 In many cases, a rhomboid pattern slowly grows on the sediment surface, as illustrated
209 by figure 5. The time needed to reach a quasi-static regime is typically a few seconds. The
210 formation of the rhomboid pattern does not involve any visible intermediate structure. On
211 the larger part of the field of view, the pattern is regular enough to measure its wavelength
212 and an inclination with respect to the mean flow. As already noted by *Karcz and Kersey*
213 [1980], the sand waves are not generated by any obvious initial perturbation, although
214 they can be artificially generated by digging a small hole in the sand (or by making a small
215 sand bump). Every pattern we observed migrated slowly downwards (typically at 0.5 to
216 1 mm s^{-1}), a characteristic also observed in the field [*Hoyt and Henry, 1963*]. Once the
217 equilibrium shape is reached, the rhomboid pattern can be described as the criss-crossing
218 of inclined straight lines, each line corresponding to a sharp front in the sediment-surface
219 elevation. This front is the lee side of a sandbank, while the stoss side is gently sloping
220 between two fronts (see figure 6). The height of this bedform scarcely ever exceeds a
221 millimeter, and remains generally small as compared to flow depth. Figure 7 shows
222 examples of the various wavelengths and angles we observed for the rhomboid pattern.
223 The angle varied between 10° and 90° . The wavelength was usually a few centimeters, or
224 a few tens of centimeters.

225 The last type of bedform that formed during our experiment were sandwaves perpen-
226 dicular to the main flow (at least initially), which will be named *ripple* hereafter, even
227 though there is no universal definition for this term [*Coleman and Eling, 2000; Charru*
228 *and Mouilleron-Arnould, 2002*]. This pattern remains roughly perpendicular to the flow,
229 although secondary instabilities may deform its initially regular shape. At the highest
230 Reynolds numbers, such deformations of the ripples could lead to triangular structures.

231 However, both their shape and their obvious relation with initially transverse sandwaves
232 allowed us to discriminate between them and true rhomboid patterns. The ripple wave-
233 length in our experiment was typically a few centimeters. They usually form alone, but
234 we have observed them in association with a rhomboid pattern, as shown on figure 7c.
235 Ripples and rhomboid pattern thus behave as independent structures. However, when
236 the angle of the rhomboid pattern tends to 90° , it becomes impossible to discriminate
237 between the two types of bedforms.

3.2. Influence of the experimental parameters

238 The shape of the rhomboid pattern changes as the slope, the discharge and the viscos-
239 ity are varied. Figure 8 expresses this dependence with respect to six non-dimensional
240 parameters. However, our exploratory experiments allowed us to vary only three param-
241 eters independently. Definitive experiments should isolate the parameter variations, for
242 instance by means of different grains size and adjustable channel width. For that reason,
243 and in order to identify the most significant correlations, we have computed Spearman's
244 rank correlation coefficient for each graph (the rank correlation coefficient is more rele-
245 vant than the classical correlation coefficient when one do not expect any specific relation
246 [*Spearman*, 1904]). The product of the correlation coefficient for the angle by the corre-
247 lation coefficient for the wavelength then quantifies the influence of a parameter on the
248 pattern shape (table 2). In Figure 8, the plots are ordered from strong to weak correlation
249 (this order remains unchanged if the classical correlation coefficient is used instead of the
250 rank correlation).

251 The parameter influencing most the pattern shape is the Froude number, as suggested
252 initially by *Woodford* [1935]. The pattern angle decreases from about 85° to about 10° as

253 the Froude number increases from 0.5 to 2.5. Varying the Froude number thus induces
254 a shift from almost transverse bedforms to elongated rhombus. Increasing the Froude
255 number also induces an increase in the pattern (non-dimensional) wavelength, from about
256 2 to a few tens.

257 The influence of the channel slope on the pattern shape is similar to that of the Froude
258 number, although the correlation is weaker. This is most likely due to the nature of our
259 arrangements, which impose a relation between slope and Froude number. The slope-
260 Froude number effects are sorted out on figure 10.

261 As the Shields parameter decreases from about 0.7 to about 0.45, the pattern angle
262 increases. From 0.45 to 0.2, the data are separated into two sets, one with a roughly
263 constant angle of about 25° , the other showing a increase form 40° to 85° as the Shields
264 parameter decreases. As this parameter increases, the non-dimensional wavelength also
265 increases, although the scatter is wide. The lowest value of the Shields parameter on these
266 plots (about 0.22) does not correspond to a global threshold for sediment transport, but
267 rather to the absence of any bed instability.

268 At low values of the Reynolds number (below 100), the pattern angle can be anything
269 between 15° and 85° . However, its range shrinks as the Reynolds number increases, to the
270 point that only elongated patterns are observed at Reynolds numbers larger than about
271 300. The Reynolds number also presents a weak positive correlation with the pattern
272 wavelength.

273 The flow aspect ratio is poorly correlated with the pattern shape. Deeper flows tend to
274 form shorter and less elongated rhombus.

275 Finally, the influence of the Weber number on the pattern is very weak. At higher
 276 Weber numbers, the pattern seems to be more elongated, and to present a slightly larger
 277 wavelength. One cannot conclude from the weakness of this correlation that capillary
 278 forces have no effect on the bedforms, only that our experiments were not designed to
 279 evaluate this influence.

280 Since only three parameters were varied during the experiment, we will hereafter present
 281 our results in terms of the three parameters which have the strongest influence on the
 282 pattern, namely F , S and θ .

283 Figure 9 illustrates in more detail the dependence of the pattern angle with respect to the
 284 Froude number. Even though Woodford's theory reproduces qualitatively the dependence
 285 of the angle with respect to the Froude number, the curve corresponding to relation (1)
 286 unquestionably lies outside the experimental error bars. However, an empirical relation
 287 inspired from equation (1), namely

$$288 \quad \alpha \approx \arcsin \frac{0.463}{F}, \quad (5)$$

289 provides a reasonably good fit to the data. This empirical curve tends to $\alpha = 90^\circ$ (that
 290 is, a ripple-like pattern) around $F = 0.463$. Figure 9 clearly shows that a rhomboid
 291 pattern can develop in a subcritical flow (that is, for a Froude number below one), in
 292 contradiction with Woodford's theory. Our experiments thus show that the rhomboid
 293 pattern does not result from stationary waves forming in supercritical flows. One could
 294 include capillary forces into Woodford's theory, by replacing the Froude number in relation
 295 (1) with U/c , where c is the celerity of gravity-capillary waves in shallow water. However,
 296 since capillarity makes the surface waves faster, this would lead to predictions further
 297 away from the data.

298 The diagram of figure 10 provides an explanation for the apparent contradiction between
299 our results and those of *Karcz and Kersey* [1980]. Indeed, these authors observed no
300 rhomboid pattern below the curve $S = 3/Re$, which corresponds to the vertical line $F = 1$
301 in the (F, S) -plane. On the contrary, we obtained many rhombi in subcritical flows when
302 the water was mixed with glucose. Except for one exception, we did not observe any
303 subcritical rhombus without glucose. This result indicates that subcritical rhombi appear
304 extremely seldom if the water viscosity is not increased. Therefore *Karcz and Kersey*,
305 using only unmixed water, were unlikely to observe any subcritical rhombus.

306 Even though the pattern shape depends mostly on the Froude number, the role of the
307 channel slope cannot be neglected, as illustrated in figure 11. If the Froude number varies
308 while the slope is fixed to 0.015 (circles), the relation between the pattern angle and
309 the Froude number shows less dispersion than in figure 8. If the slope is fixed to 0.03
310 (squares), the correlation remains, but the whole curve is shifted downwards with respect
311 to the previous case. Finally, when the slope is fixed to 0.05 (disks), the data still line up
312 onto the continuation of the previous relation. Thus, the pattern angle is not a function of
313 the Froude number only, and part of the dispersion observed in figure 11 can be ascribed
314 to variations in the channel slope.

315 *Hoyt and Henry* [1963] related the rhombus aspect ratio (that is, the angle α) to the
316 slope of the beach where they formed. Their data set is rather convincing (see their figure
317 3), but they did not measure the Froude number, which is likely to change both with
318 the location of the measurements, and during the pattern formation. The affine relation
319 between α and S they propose probably results from a correlation between the slope and
320 the other flow parameters. It might still be used as an indicator of the paleo-environment,

321 but the data on which it is based are not sufficiently controlled for their conclusion to
 322 hold in the general case.

3.3. Dynamics of the bedforms

323 Our experiments highlight the limitations of theories based on supercritical surface
 324 waves. We suspect that their main flaw is to consider only the fluid flow, without cou-
 325 pling it to sediment transport. The present section is devoted to the evaluation of this
 326 proposition. Indeed, bedload transport is slow as compared to the water velocity. Conse-
 327 quently, if the sediment transport is strongly coupled to the flow, the typical time scale
 328 of the bedforms dynamics should be controlled by bedload transport.

Rhomboid patterns typically have a steep lee side, and a gently sloping stoss-side (figure 6). Let us denote by h_+ and h_- the elevation of the rhombus crest, and the elevation of its bottom (figure 12). Similarly, q_{s+} and q_{s-} denote respectively the sediment flux at the crest and at the bottom (the sand compaction is included in this definition). Now, if the pattern has reached a steady state and moves at velocity c_r , the sediment mass balance reads

$$c_r (h_+ - h_-) = q_{s+} - q_{s-}. \quad (6)$$

329 The above equation is the integral of the Exner equation.

330 At the lowermost point of the pattern, the grains are sheltered from the flow, and one
 331 can expect the bedload to be very low there. Although we have no strict evidence for such
 332 a statement, the grains indeed seemed immobile to the eye near the bottom of the pattern
 333 during the experiments. We will assume hereafter that $q_{s-} \approx 0$ as a first approximation.

334 Now, the average sediment discharge Q_s measured during some of the experiments
 335 provides a rough approximation for the bedload transport upstream of the crest, that is

336 $q_{s+} \approx Q_s/W$. Thus, assuming further that the front amplitude $\delta h = h_+ - h_-$ does not
337 vary much between experimental runs, the pattern velocity c_r should be strongly related
338 to the average sediment discharge.

339 One can extract the pattern velocity from the photographs of the bed taken at regular
340 time intervals. This procedure requires that the pattern can be recognized unambiguously
341 on a sufficient number of successive pictures. This constraint, in addition to the difficulty
342 in measuring the sediment discharge (see section 2.1) reduces greatly the quantity of data.

343 Figure 13 shows the pattern velocity as a function of the sediment discharge, when
344 both quantities can be measured. Despite the small number of data points, the two
345 quantities appear to be strongly correlated (the correlation coefficient is 0.85). The best
346 linear fit gives an average value of $\delta h = 0.49$ mm for the front amplitude, which is
347 correct to well within an order of magnitude. This result is clearly preliminary, since it
348 concerns a quantity that is not easy to measure precisely, and which can be predicted by
349 no theory. However, it supports the idea that the time scale involved in the rhomboid
350 pattern dynamics is that of bedload transport.

351 If a quantitative model of the rhomboid pattern can be elaborated, the tight relation
352 between the rhomboid pattern and sediment transport could be used to test transport
353 models, as ripples have been used (see for example *Charru* [2006]). The rhomboid pattern
354 provides one more measurable quantity than the ripples, namely their opening angle. This
355 point could prove essential when tackling the difficult issue of the lateral slope effect on
356 sediment transport.

4. Discussion and conclusion

357 The present paper reports experimental investigations of the rhomboid pattern. It is
358 demonstrated that bedforms similar to the rhombus commonly found on beaches can de-
359 velop spontaneously on a granular bed activated by a thin film of flowing water. The
360 experiment is fairly reproducible. The rhomboid pattern seems distinct from classical rip-
361 ples, as the two can develop independently and can be superimposed on one another. The
362 rhomboid pattern eventually reaches a steady state, during which it migrates downstream
363 with a homogeneous wavelength and angle.

364 Both the surprising regularity of the pattern and its existence in very viscous flows
365 are strong indications that it is a fundamental morphodynamic instability instead of a
366 subtype or a precursor of classical ripples, although there is no definitive evidence yet
367 in support of this statement. In other words, our experiments tend to indicate that the
368 distinction between rhombus and ripple, well established on morphological grounds alone,
369 is also justified in genesis.

370 Among the various theories proposed in the literature to explain the formation of rhom-
371 bus, Woodford's has been the most durable, and many others are variants of it. This
372 theory states that the rhomboid beach pattern can form only in supercritical flows. Our
373 experiments demonstrate that it is not in general the case, even though the claim holds
374 if the fluid viscosity is that of pure water. Since Woodford's model (as well as any other
375 associated with hydraulic jumps or gravity waves) crucially requires that the Froude num-
376 ber be larger than 1.0, our result indicates that the rhomboid pattern formation is not yet
377 fully understood. Nevertheless, for paleo-environmental purposes, one may still consider

378 the presence of rhomboid beach pattern as an indicator of super-critical flows, as long as
379 the fluid involved in their formation is pure water.

380 The dynamics of the experimental rhomboid pattern provides some indications for future
381 theories. Indeed, the typical velocity of this bedform scales with the sediment transport
382 rate, indicating that a complete theory should take sediment transport into account, as
383 opposed to considering the flow only. In other words, our results tend to indicate that
384 the rhomboid pattern is not simply the passive mark of some flow structures, but rather
385 results from the coupling between the flow and the granular bed. If this is confirmed,
386 the rhomboid pattern could become an assessment tool for bedload transport models, a
387 subject of intense present research [*Vanoni, 2006; Parker et al., 2003; Charru et al., 2004*].

388 A quantitative model of the rhomboid pattern would also shed light on the role of vis-
389 cosity in their formation. Are the patterns in sub-critical flows distinct from the classical
390 super-critical ones, the viscosity selecting one type or the other? If so, does turbulent
391 bulk viscosity have the same effect on a large-scale rhomboid pattern, as suggested by
392 a referee of the present paper? Those are questions that require both more experiments
393 and a comprehensive theory. Resembling structures formed by laminar and by turbulent
394 flows are not uncommon in geomorphology [*Lajeunesse et al., 2010*], and their comparison
395 might improve our understanding of both.

396 The spontaneous emergence of a homogeneous pattern from an initially flat bed, in a
397 reproducible experiment, strikes us as an indication of a linear instability. If this is true,
398 the linear stability analysis of a coupled sediment-flow model should provide an answer to
399 the question of the rhomboid pattern angle. In theory, it could also predicts the pattern
400 wavelength, a characteristic easily measured but predicted by none of the extant theories.

401 We gave this idea an initial trial using the shallow-water equations to model the water
402 flow, but the associated predictions did not match the data any better than Woodford's
403 theory. A three dimensional model is the subject of present research.

404 **Acknowledgments.** It is our pleasure to thank Clément Narteau, Stéphane Zaleski,
405 François Charru, Philip Hall, Alexander Petroff and Philippe Claudin for fruitful discus-
406 sions. We also wish to express appreciation to Brandon McElroy and Paul Carling for
407 their helpful suggestions about the bibliography, as well as to Antonio Vieira and Yves
408 Gamblin for the building of the experimental set-up.

Appendix: Comment on Chang and Simons' theory

409 When Chang and Simons state that "*the unsteady terms in the [...] equations can be*
410 *neglected*" [Chang and Simons, 1970, 493], they unduly extend a common hypothesis
411 in Geomorphology, namely that the sediment transport time-scale is much larger than
412 the dynamical time of the flow. Indeed, this hypothesis allows one to neglect the time
413 derivatives in the flow equations, but on no account can it be used to neglect time in
414 the Exner equation [Parker, 1976]. By doing so, Chang and Simons [1970] reduce their
415 model to a classical hydraulic model that does not take sediment motion into account.
416 Consequently, they could as well remove their equation (8) and not consider the sediment
417 flux q_1 as a variable.

418 The above remark implies that Chang and Simons [1970] use the hydraulic model of
419 Woodford [1935], and thus should end up with the same formula for the static wave
420 angle α . A mistake in their analysis lead them to propose $\alpha = \arctan(1/F)$ instead of

421 Woodford's $\alpha = \arcsin(1/F)$. Indeed, on page 494, the authors define the determinant

$$422 \quad N = \begin{vmatrix} u & w & 0 & 0 & g & 0 & 0 & 0 \\ 0 & 0 & u & w & 0 & g & 0 & 0 \\ h & 0 & 0 & h & u & w & 0 & 0 \\ 0 & \frac{wq_1}{u^2} & 0 & -\frac{q_1}{u} & 0 & 0 & -1 & -\frac{w}{u} \\ dx & dz & 0 & 0 & 0 & 0 & 0 & 0 \\ 0 & 0 & dx & dz & 0 & 0 & 0 & 0 \\ 0 & 0 & 0 & 0 & dx & dz & 0 & 0 \\ 0 & 0 & 0 & 0 & 0 & 0 & dx & dz \end{vmatrix} \quad (7)$$

423 where h , u , w and q_1 are the flow depth, the downstream velocity, the transverse velocity,
424 and the longitudinal sediment flux, respectively. The elementary displacements dx , dy
425 and dz correspond to longitudinal, transverse and vertical directions. Later, the authors
426 present equation (13), namely

$$427 \quad (wdx - udz)^2 ((wdx - udz)^2 - gh(dx)^2) = 0, \quad (8)$$

428 as a condition for N to vanish. The correct equation is actually

$$429 \quad (wdx - udz)^2 (dz^2 (gh - u^2) + 2 dx dz uw + dx^2 (gh - w^2)) = 0. \quad (9)$$

430 In turns, this imposes

$$431 \quad \frac{dx}{dz} = \pm \sqrt{\frac{u^2}{gh} - 1} \quad (10)$$

432 instead of their equation (15), for a vanishing transverse velocity W . Given that $dx/dz =$
433 $1/\tan(\alpha)$, one recovers Woodford's formula after some arithmetic.

References

- 434 Allen, J. R. L. (1982), *Sedimentary Structures—Their Character and Physical Basis*, Vol.
435 I, *Developments in Sedimentology*, 30b. Elsevier, Amsterdam, 663, 395–405.
- 436 Barenblatt, G. (1996), *Scaling, Self-similarity, and Intermediate Asymptotics: Dimensional Analysis and Intermediate Asymptotics*, 386 pp., Cambridge Univ Pr.

- 438 Best, J. (1992), On the entrainment of sediment and initiation of bed defects: insights from
439 recent developments within turbulent boundary layer research, *Sedimentology*, *39*(5),
440 797–811.
- 441 Chang, H. Y., and D. B. Simons (1970), The bed configuration of straight sand beds when
442 flow is nearly critical, *Jour. Fluid Mech.*, *42*, 491–495.
- 443 Charru, F. (2006), Selection of the ripple length on a granular bed sheared by a liquid
444 flow, *Physics of Fluids*, *18*, 121,508, doi:10.1063/1.2397005.
- 445 Charru, F., and H. Mouilleron-Arnould (2002), Instability of a bed of parti-
446 cles sheared by a viscous flow, *Journal of Fluid Mechanics*, *452*, 303–323, doi:
447 10.1017/S0022112001006747.
- 448 Charru, F., H. Mouilleron, and O. Eiff (2004), Erosion and deposition of particles
449 on a bed sheared by a viscous flow, *Journal of Fluid Mechanics*, *519*, 55–80, doi:
450 10.1017/s0022112004001028.
- 451 Coleman, S. E., and B. Eling (2000), Sand wavelets in laminar open-channel flows, *Journal*
452 *of Hydraulic Research/Journal de Recherches Hydraulique*, *38*(5), 331–338.
- 453 Collinson, J., and D. Thompson (1982), *Sedimentary structures*, 194 pp., Allen & Unwin
454 Australia.
- 455 Daerr, A., P. Lee, J. Lanuza, and É. Clément (2003), Erosion patterns in a sediment layer,
456 *Physical Review E*, *67*(6), 65,201, doi:10.1103/PhysRevE.67.065201.
- 457 Devauchelle, O., C. Josserand, and S. Zaleski (2007), Forced dewetting on porous media,
458 *Journal of Fluid Mechanics*, *574*, 343–364, doi:10.1017/S0022112006004125.
- 459 Devauchelle, O., L. Malverti, É. Lajeunesse, F. Métivier, P.-Y. Lagrée, C. Josserand,
460 and S. Zaleski (2008), Erosion shock wave in laminar flumes, in *Proceedings of Marine*

- 461 *and River Dune Dynamics III, International Workshop*, vol. III, edited by D. Parsons,
462 T. Garlan, and J. Best, pp. 59–62, University of Leeds, UK.
- 463 Docoslis, A., R. F. Giese, and C. J. van Oss (2000), Influence of the water–air interface on
464 the apparent surface tension of aqueous solutions of hydrophilic solutes, *Colloids and*
465 *Surfaces B: Biointerfaces*, 19(2), 147–162.
- 466 Gyr, A., and A. Schmid (1989), The different ripple formation mechanism, *Journal of*
467 *Hydraulic Research*, 27(1), 61–74.
- 468 Hoyt, J. H., and V. J. Henry (1963), Rhomboid ripple mark, indicator of current direction
469 and environment, *Journal of Sedimentary Research*, 33(3), 604–608.
- 470 Ikeda, H. (1983), Experiments on bedload transport, bed forms, and sedimentary struc-
471 tures using fine gravel in the 4-meter-wide flume, *Environmental Research Center papers*,
472 2, 1–78.
- 473 Johnson, D. W. (1919), *Shore Processes and Shoreline Development*, pp. 514–517, John
474 Wiley & Sons, Inc.
- 475 Karcz, I., and D. Kersey (1980), Experimental Study of Free-Surface Flow Instability and
476 Bedforms in Shallow Flows, *Sedimentary Geology*, 27(4), 263–300.
- 477 Lajeunesse, E., L. Malverti, P. Lancien, L. Armstrong, F. Metivier, S. Coleman, C. Smith,
478 T. Davies, A. Cantelli, and G. Parker (2010), Fluvial and subaqueous morphodynamics
479 of laminar and near-laminar flows, *Sedimentology*, *in press*.
- 480 Malverti, L., É. Lajeunesse, and F. Métivier (2008), Small is beautiful: upscaling from
481 microscale laminar to natural turbulent rivers, *Journal of Geophysical Research-Earth*
482 *Surface*, 113(F4), F04,004, doi:10.1029/2007JF000974.

- 483 McMullen, R. M., and D. J. P. Swift (1967), An occurrence of large-scale rhomboid ripples,
484 Minas Basin, Nova Scotia, *Journal of Sedimentary Research*, *37*(2), 705–706.
- 485 Morton, R. A. (1978), Large-scale rhomboid bed forms and sedimentary structures asso-
486 ciated with hurricane washover, *Sedimentology*, *25*, 183–204.
- 487 Orszag, S., and L. Kells (1980), Transition to turbulence in plane Poiseuille and plane
488 Couette flow, *J. Fluid Mech.*, *96*, 159–205.
- 489 Otvos, E. G. (1965), Types of rhomboid beach surface patterns, *American Journal of*
490 *Science*, *263*(3), 271–276.
- 491 Parker, G. (1976), On the cause and characteristic scales of meandering and braiding in
492 rivers, *Journal of Fluid Mechanics*, *76*, 457–480.
- 493 Parker, G., G. Seminara, and L. Solari (2003), Bed load at low Shields stress on arbitrarily
494 sloping beds: Alternative entrainment formulation, *Water Resources Research*, *39*(7),
495 1183, doi:10.1029/2001WR001253.
- 496 Singh, I. B. (1969), Primary sedimentary structures in Precambrian quartzites of Tele-
497 mark, southern Norway and their environmental significance, *Norsk geologisk tidsskrift*,
498 *49*, 1–31.
- 499 Spearman, C. (1904), The proof and measurement of association between two things, *The*
500 *American Journal of Psychology*, *15*(1), 72–101.
- 501 Stauffer, M. R., Z. Hajnal, and D. J. Gendzwill (1976), Rhomboidal lattice structure: a
502 common feature on sandy beaches, *Canadian Journal of Earth Sciences*, *13*(12), 1667–
503 1677.
- 504 Straaten, L. (1953), Megaripples in the Dutch Wadden Sea and in the Basin of Arcachon
505 (France), *Geologie Mijnb*, *15*, 1–11.

- 506 Thompson, W. O. (1949), Lyons sandstone of Colorado Front Range, *AAPG Bulletin*,
507 *33*(1), 52–72.
- 508 Vanoni, V. A. (2006), *Sedimentation Engineering: Theory, Measurements, Modeling, and*
509 *Practice, Manuals and Reports on Engineering Practice*, vol. 54, 424 pp., American
510 Society of Civil Engineers, USA.
- 511 Venditti, J., M. Church, and S. Bennett (2005), Bed form initiation from a flat sand bed,
512 *J. Geophys. Res.-Earth Surf.*, *110*(F1), doi:10.1029/2004JF000149.
- 513 Williamson, W. C. (1887), On Some Undescribed Tracks of Invertebrate Animals from
514 the Yoredale Rocks, and on some Inorganic Phenomena, Produced on Tidal Shores,
515 Simulating Plant Remains, *Manchester Literary and Philosophical Society, Memoirs*
516 *and Proceedings*, *3*(10), 19–29.
- 517 Woodford, A. O. (1935), Rhomboid ripple mark, *Amer. Jour. Science*, *29*(174), 518–525.



Figure 1. Rhomboid beach pattern on the beach at Goleta, California. Such features form on the swash zone, when a thin film of water returns to sea. Here the structure is visualized by the segregation between grains of different colors. The short dimension of the card is 5.4 cm.

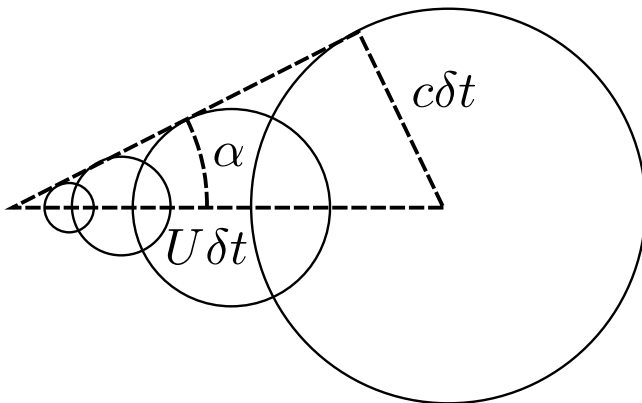


Figure 2. Scheme of the gravity wave propagation in a super-critical flow. A perturbation propagates in all directions at velocity c , while it is transported by the mean flow at velocity U . For super-critical flows (that is, for $c > U$), the angle α of the wave envelope satisfies the relation $\sin(\alpha) = c/U = 1/F$, where F is the Froude number. *Woodford* [1935] first suggested that such stationary waves could produce the rhomboid pattern.

Mechanism	Angle expression	References
Two sets of superimposed ordinary ripples		<i>Williamson</i> [1887]
Stationary wave in a supercritical flow (see figure 2)	$\alpha = \arcsin(1/F)$	<i>Woodford</i> [1935]
Drainage trough deposited sand (no surface flow required)		<i>Stauffer et al.</i> [1976]
Hydraulic jumps	$\alpha = \arctan(1/F)$ corrected to $\alpha = \arcsin(1/F)$ in the present Appendix	<i>Chang and Simons</i> [1970]; <i>Allen</i> [1982]
Interaction between anti-dunes and longitudinal striations	$\alpha = \arctan(1/(\pi F^2))$ (in turbulent flows)	<i>Ikeda</i> [1983]
Moving contact line instability		<i>Devauchelle et al.</i> [2007]

Table 1. Different theories for the formation of the rhomboid pattern, by order of publication.

An extensive review was presented by *Allen* [1982].

Pattern property	F	S	θ	Re	R_f	We
α	-0.878	-0.755	-0.729	-0.663	0.441	-0.472
λ/D	0.583	0.685	0.512	0.348	-0.521	0.165

Table 2. Correlation matrix for the dependence of the pattern angle and wavelength on six non-dimensional parameters. The coefficients correspond to Spearman's rank correlation.

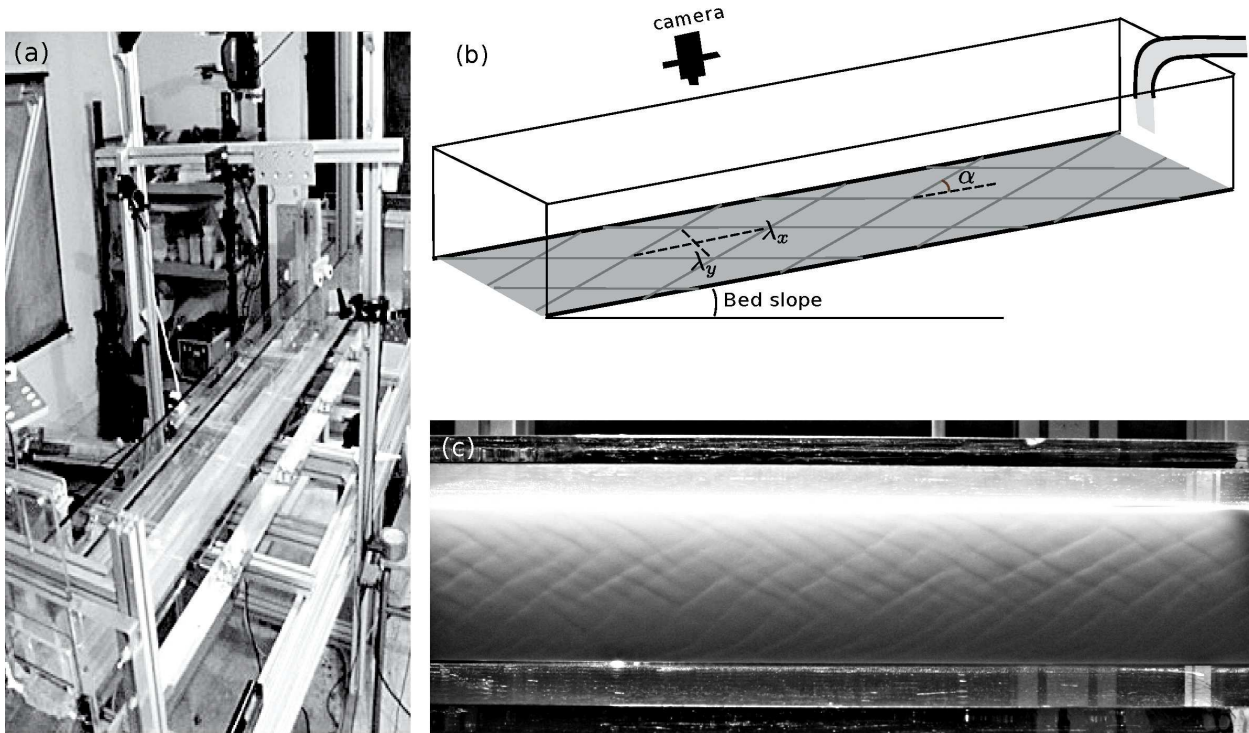


Figure 3. (a) Picture of the experimental arrangement. The glass channel is filled with silica grains, above which a thin film of water flows. Pictures of the bedforms are taken from above. (b) Schematic of the experimental setup, showing the definition of the rhomboid pattern angle and wavelengths. (c) Example of observed rhomboidal bedforms (flow is from right to left).

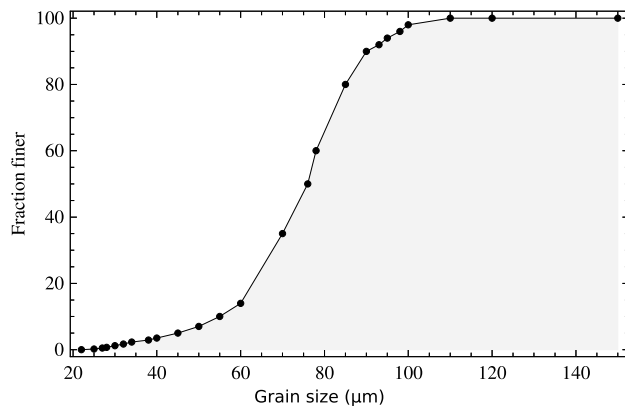


Figure 4. Cumulative distribution function of the sediment used in the experiment. The median grain diameter d_s is about $75 \mu\text{m}$.

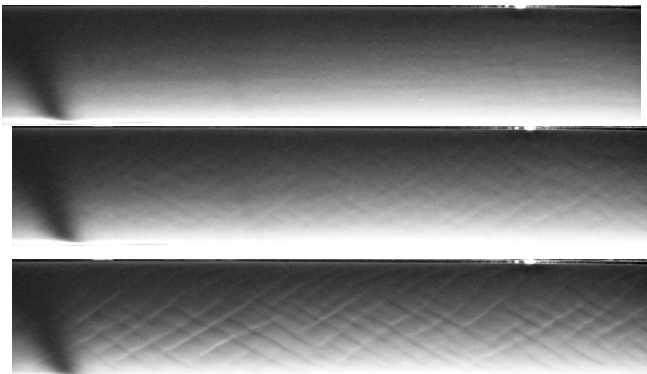


Figure 5. Development of a rhomboid instability on the granular bed of a laminar channel (flow is from right to left). From top to bottom, the pictures were taken at times $t = 0$ s, $t = 90$ s and $t = 282$ s respectively. The pattern develops roughly uniformly in terms of amplitude, angle and wavelength. Its formation does not involve ripples. For this run, $F = 1.1$, $S = 0.022$, $Bo = 0.58$ and $\theta = 0.40$

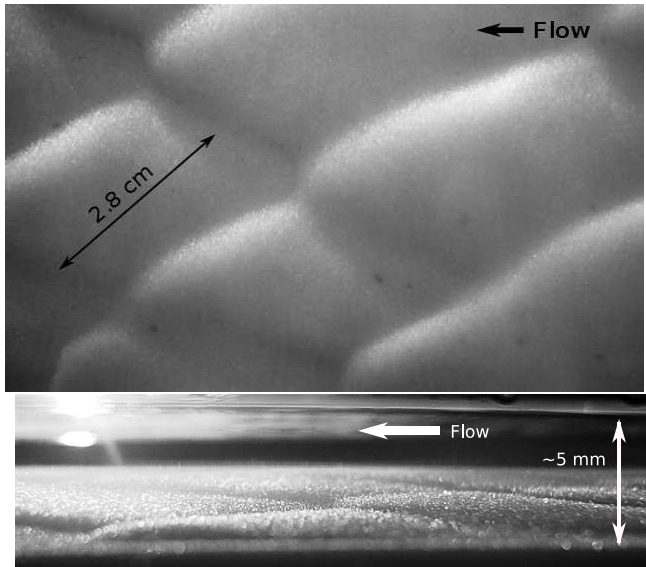


Figure 6. Close view of an experimental rhomboid pattern. *Above* : Rhomboidal pattern observed through the water surface. For this run, $F = 0.43$, $S = 0.013$, $Bo = 1.35$ and $\theta = 0.37$. *Below* : Rhomboidal pattern observed through the glass side wall of the experimental channel. The amplitude of the rhomboid pattern is of order, or less than, 1 mm.

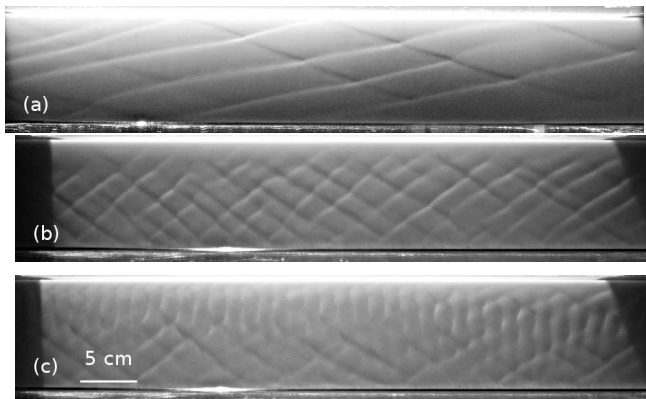


Figure 7. Various bedforms observed in our experiment (flow is from right to left). (a) Large rhomboid pattern ($F = 1.76$, $S = 0.03$ and $\theta = 0.616$). (b) Small rhomboid pattern ($F = 0.95$, $S = 0.015$ and $\theta = 0.485$). (c) Rhomboid pattern mixed with ripples ($F = 1.01$, $S = 0.015$ and $\theta = 0.504$).

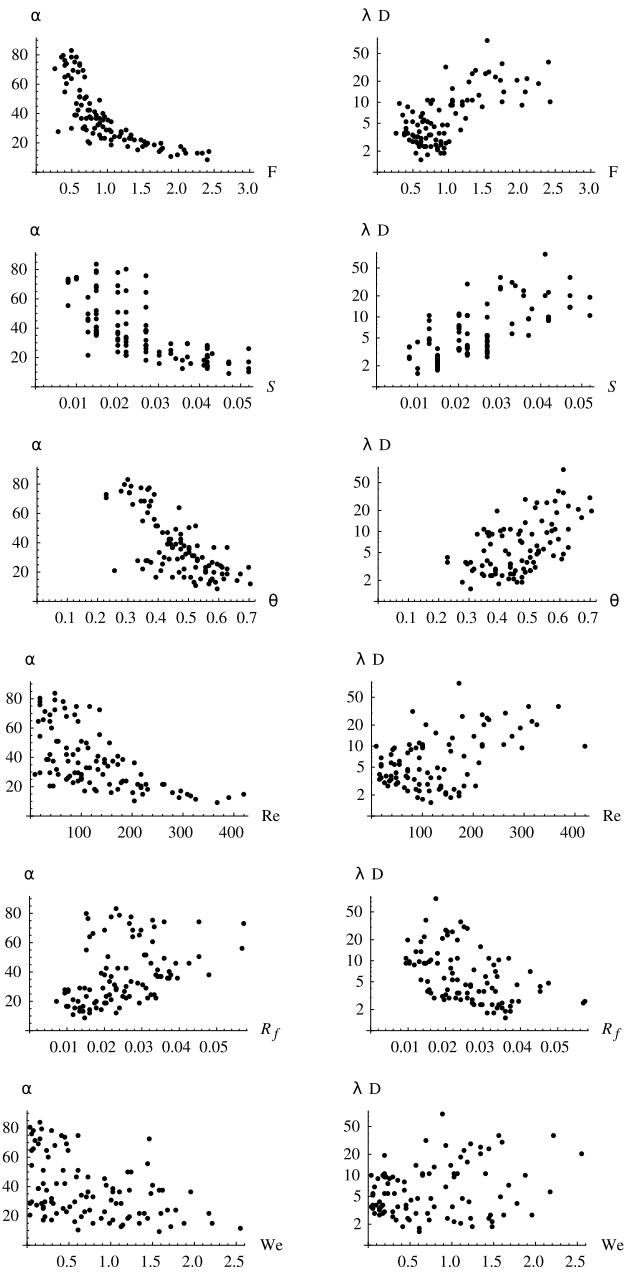


Figure 8. Geometrical properties of the rhomboid pattern (angle α and non-dimensional wavelength λ/D) versus various non-dimensional parameters. The complete set of experiments is represented here.

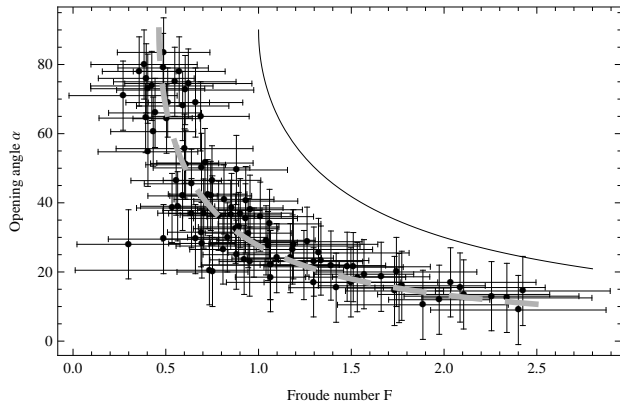


Figure 9. Rhomboid pattern angle as a function of the Froude number. Complete set of experimental results, with error bars. Black solid line: relation (1), corresponding to the theory of *Woodford* [1935]. Thick gray dashed line: best fit corresponding to relation (5).

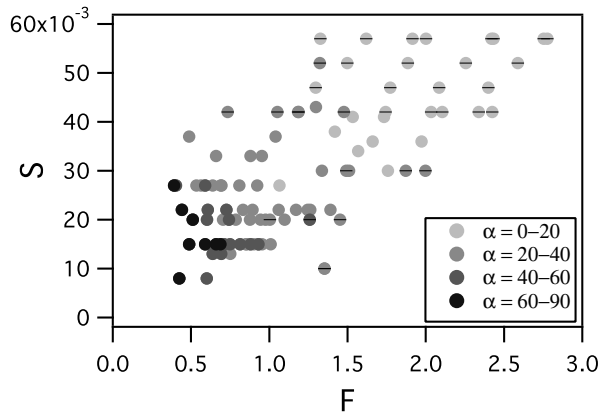


Figure 10. Existence diagram of the rhomboid instability, versus the Froude number F and the channel slope S . The gray scale indicates the angle of the corresponding pattern, and thus may be used to discriminate between ripples and rhomboid structures. The dashed disks represent data obtained with pure water, whereas the fluid viscosity was increased with sugar otherwise.

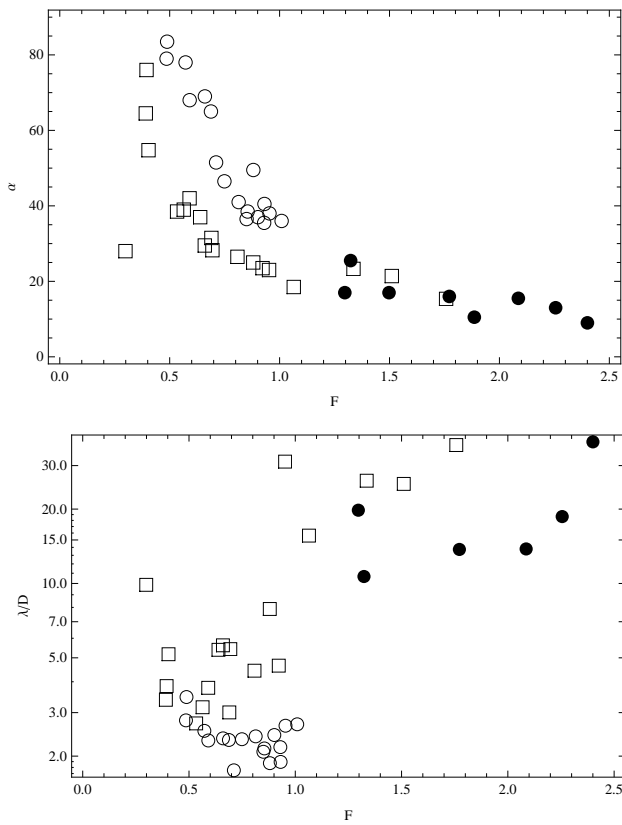


Figure 11. Influence of the Froude number on the rhomboid pattern, at fixed slope. Circles: $S = 0.015 \pm 10\%$; square: $S = 0.03 \pm 10\%$; disks: $S = 0.05 \pm 10\%$.

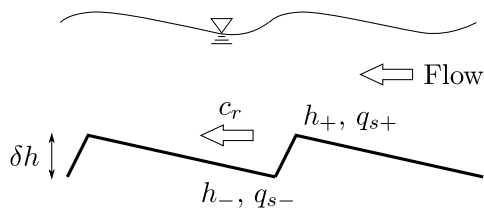


Figure 12. Longitudinal section of the rhomboid pattern.

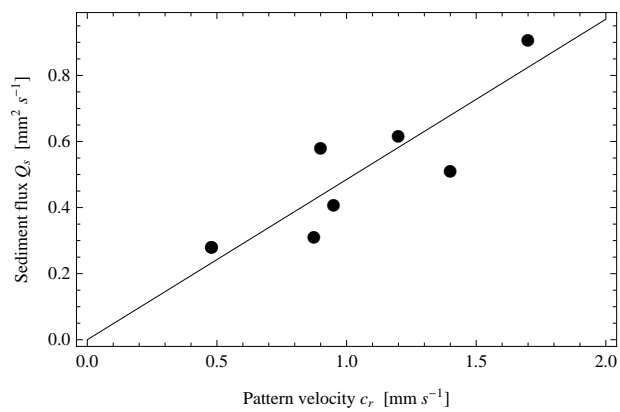


Figure 13. Measured dimensional sediment flux versus measured pattern velocity. The solid line represents the best linear fit, $Q_s = c\delta h$, with $\delta h = 0.49$ mm.